ACS Catalysis

Research Article

pubs.acs.org/acscatalysis

Acid–Base Reactivity of Perovskite Catalysts Probed via Conversion of 2-Propanol over Titanates and Zirconates

Guo Shiou Foo,[†,§] Felipe Polo-Garzon,[†,§] Victor Fung,[‡] De-en Jiang,[‡] Steven H. Overbury,[†] and Zili Wu*[,†]

[†]Chemical Sciences Division and Center for Nanophase Materials Sciences, Oak Ridge National Laboratory, Oak Ridge, Tennessee 37831, United States

[‡]Department of Chemistry, University of California, Riverside, California 92521, United States

Supporting Information

ABSTRACT: Although perovskite catalysts are well-known for their excellent redox property, their acid–base reactivity remains largely unknown. To explore the potential of perovskites in acid–base catalysis, we made a comprehensive investigation in this work on the acid–base properties and reactivity of a series of selected perovskites, $SrTiO_3$, $BaTiO_3$, $SrZrO_3$, and $BaZrO_3$, via a combination of various approaches including adsorption microcalorimetry, in situ FTIR spectroscopy, steady state kinetic measurements, and density functional theory (DFT) modeling. The perovskite surfaces are shown to be dominated with intermediate and strong basic sites with the presence of some weak Lewis acid sites, due to the preferred exposure of SrO/BaO on the perovskite surfaces as evidenced by low energy ion scattering (LEIS) measurements. Using the conversion of 2-propanol as a probe reaction, we found that the reaction is more selective to dehydrogenation over dehydration due to the dominant surface basicity of the perovskites. Furthermore, the adsorption energy of 2-propanol ($\Delta H_{ads,2-propanol}$) is found to be related to both a bulk property (tolerance factor) and the synergy between surface acid and base sites. The results from in situ FTIR and DFT calculations suggest that both dehydration and dehydrogenation reactions occur mainly through the E_{1cB} pathway, which involves the deprotonation of the alcohol group to form a common alkoxy intermediate on the perovskite surfaces. The results obtained in this work pave a path for further exploration and understanding of acid–base catalysis over perovskite catalysts.

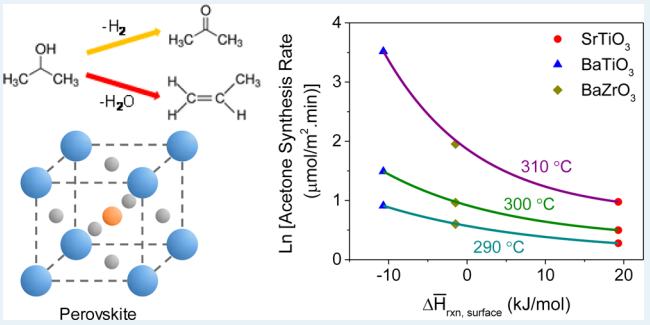

KEYWORDS: *heat of adsorption, surface termination, heat of reaction, dehydration, dehydrogenation*

1. INTRODUCTION

Perovskite is a general name for mixed metal oxides with the structural formula ABO_3. In the perovskite structure, the A cation is typically a lanthanide, alkaline or alkaline-earth cation, while the B cation is usually a transition metal cation.[1] An ideal perovskite unit cell can be described as cubic, and belonging to the *Pm*3*m* space group, where the A cation is 12-fold coordinated to oxygen anions, and the B cation is 6-fold coordinated to oxygen anions.[2]

One of the main advantages of the perovskite structure is its flexibility to adopt a wide range of compositions. This is possible by partially or fully substituting either the A or B cation, resulting in different surface and redox properties.[3] However, the nature and extent of substitution of the A and/or B cation is limited by the stability of the framework. The Goldschmidt tolerance factor (t) is used to determine the geometric constraint and distortion of the crystal structure, and it should meet the restriction of $0.75 \leq t \leq 1.0$, where $t = (r_A + r_O)/[2^{1/2}(r_B + r_O)]$, and r_A, r_B, and r_O are the radii of the respective ions.[4] An ideal cubic perovskite structure has a tolerance factor of 1. If the value of t is less than 0.75 or more than 1.00, the crystal structure typically becomes unstable.

Early studies on the catalysis of perovskites were focused on the reduction of NO and alkenes, exhibiting exceptional catalytic activity.[5,6] Coupled with its low cost, perovskites have the potential of replacing noble metals in catalytic convertors. The catalytic reduction of NO uses CO,[7] NH_3,[8] hydrocarbons,[9] or H_2[10] as reducing agents. It was reported that the redox ability of the B cation and the presence of oxygen vacancies are required for the adsorption and activation of NO.[11,12] Furthermore, partial substitution of the B cation can improve its catalytic activity. Kaliaguine et al. reported that the partial substitution of Fe by Cu or Pd in $LaFe_{1-x}(Cu, Pd)_xO_3$ resulted in enhanced reduction of NO in the presence of C_3H_6.[13] It was suggested that this was due to the increased

Received: March 10, 2017
Revised: May 19, 2017
Published: May 23, 2017

DOI: 10.1021/acscatal.7b00783
ACS Catal. 2017, 7, 4423–4434

concentration of oxygen vacancies and enhanced reducibility of the cation.

Besides reduction, perovskite catalysts are also active in oxidation reactions. It was reported that manganite and cobaltite perovskites are active in the catalytic oxidation of carbon monoxide and methane.[3,14] Although PdO is an active catalyst for CH_4 oxidation, it can be deactivated by decomposition.[15] Furthermore, it deactivates rapidly at high temperature compared to perovskites.[16] Similarly, the catalytic performances of perovskites can be tuned by partial substitution of the A and/or B cation. Ponce et al. synthesized a series of $La_{1-x}Sr_xMnO_3$ manganites and reported that the substitution $x = 0.2$ exhibited the highest activity for methane combustion.[17] This was attributed to the higher stability of Mn^{4+} in the structure.

While most of the research has focused on reduction and oxidation reactions over perovskites, there is limited literature on the surface acid−base properties and reactions of perovskites. Trikalitis et al. varied the amount of Sr in $La_{1-x}Sr_xVO_3$ and reported that the selectivity of propene decreased with increasing Sr content in the conversion of 2-propanol.[18] It was suggested that this was due to the creation of more basic sites, but its surface properties were not reported. Similarly, $LaMnO_3$ mixed with carbon black was used in the ketonization of *n*-butanol,[19] but its acid−base properties were not investigated either. Furthermore, the catalytic effect of $LaMnO_3$ was not decoupled from carbon black. In addition, there are conflicting reports on the origin of acid−base sites on perovskites in the literature. Kuhn et al. investigated the surface properties of $La_{0.6}Sr_{0.4}Co_yFe_{1-y}O_{3-\delta}$ using methanol as a probe molecule.[20] It was demonstrated that Lewis acid sites are correlated to the Sr content, while basic sites are associated with the Co content. In contrast, Natile et al. reported that Lewis acid sites are correlated to the atomic ratio of Co to La for nanostructured $LaCoO_3$ powders.[21]

In light of the largely unknown acid−base properties of perovskites, in this work, we used the conversion of 2-propanol as a probe reaction to characterize the acid−base reactivity of perovskites with selected titanates and zirconates. In the presence of an acid or base site, 2-propanol can undergo intramolecular dehydration to form propene and water, intermolecular dehydration to form di-isopropyl ether, or dehydrogenation to form acetone and hydrogen.[22−24] The perovskites used in this study are $SrTiO_3$, $BaTiO_3$, $SrZrO_3$, and $BaZrO_3$. By characterizing the nature, density, and strength of surface acid−base sites, new insights can be obtained by comparing these to kinetic measurements. Furthermore, the adsorption of 2-propanol over the perovskites was investigated using FTIR spectroscopy, microcalorimetry, and DFT calculations. A combination of these approaches allows us to establish relationships between surface acid−base properties and the catalytic reactivity of perovskite catalysts, thereby laying the ground for the exploration and design of a perovskite catalyst with enhanced activity for acid−base reactions.

2. EXPERIMENTAL SECTION

2.1. Materials. Strontium titanate, barium titanate, and acetone (99.9%) were purchased from Sigma-Aldrich. Strontium zirconate and barium zirconate were purchased from Alfa Aesar. 2-Propanol (99.9%) was purchased from Fischer Scientific. Argon, 5% O_2/He, 5% O_2/Ar, O_2, NH_3, and CO_2 were purchased from Airgas. The four perovskite catalysts were calcined in air at 550 °C for 4 h, with a ramp rate of 10 K/min before the characterization and reactivity study.

2.2. Characterization. Nitrogen physisorption was performed using a Micromeritics Gemini 2375 Surface Area and Pore Size Analyzer at −196 °C. The catalysts were degassed for 1 h prior to measurement. The BET method[25] and the BJH method[26] were used to calculate the surface areas and pore volumes, respectively. X-ray diffraction (XRD) patterns were collected with a PANalytical X'Pert Pro system using Cu Kα radiation. Diffractograms were obtained at incident angles for $2\theta = 7-90°$. Scanning electron microscope (SEM) images were collected using a Zeiss Merlin system operating at 1.00 kV.

To quantify the concentration and strength of acid and base sites, the heat of adsorption of NH_3 and CO_2 were measured using a Micromeritics 3Flex Characterization Analyzer coupled with a Setaram Sensys Evo DSC microcalorimeter.[27] Each sample (sieved between 180 and 400 μm, 50−200 mg) was loaded into one side of a custom-made quartz bitube,[28] and the tube was inserted into the microcalorimeter aluminum block. The tube opening was connected to the chemisorption port of the 3Flex instrument for degassing and dosing. Each sample was evacuated and heated at 550 °C for 1 h, dosed with 500 mmHg of O_2, evacuated for 30 min each for two rounds, and cooled down to 150 °C (NH_3 adsorption) or 30 °C (CO_2 adsorption). The temperature was held for 1 h to reach thermal equilibrium. Subsequently, the sample was exposed to doses of NH_3 or CO_2. After the final target pressure was reached, the sample was evacuated for 1 h at the same temperature and dosed with NH_3 or CO_2 again. The concentration of acid and base sites was determined by the amount of irreversibly adsorbed NH_3 and CO_2, respectively. A separate control experiment using an empty bitube filled with quartz wool showed negligible amount of irreversible adsorption of the probe molecules.

To determine the type of acid and base sites present, pyridine and CO_2 adsorption followed by FTIR spectroscopy were performed using a Thermo Nicolet Nexus 670 FTIR spectrometer with an MCT detector. Each spectrum was recorded with 32 scans at a resolution of 4 cm^{-1}. The sample was loaded into a porous ceramic cup, and the cup was inserted into a diffuse reflectance infrared fourier transform spectroscopy (DRIFTS) cell (HC-900, Pike Technologies). The sample was activated at 550 °C for 1 h under 30 mL/min of 5% O_2/He and cooled down to 150 °C (pyridine adsorption) or 25 °C (CO_2 adsorption). The gas was switched to 30 mL/min of He, and a background spectrum was collected before any chemisorption. For pyridine adsorption, He was bubbled through a saturator filled with liquid pyridine at 25 °C. A pulse of pyridine saturated gas (sample loop 0.5 mL) was introduced into the sample cell. For CO_2 adsorption, a pulse of 2% CO_2/He was introduced into the sample cell. After adsorption, the sample was purged with He for 15 min (30 mL/min), and a spectrum was collected.

The samples were sent to Lehigh University for low energy ion scattering (LEIS) analysis to determine the composition of the top surface layer.[29,30] LEIS spectra were collected by using an IONTOF Qtac100 spectrometer (ION-TOF GmbH, Münster, Germany). Briefly, each sample was pressed into a circular self-supported wafer and transferred into a sample holder. The sample was evacuated and heated to 100 °C, and around 100 Torr of O_2 was introduced into the chamber. Subsequently, the temperature was increased to 500 °C and held for 30 min. After cooling and evacuation, the sample was

DOI: 10.1021/acscatal.7b00783
ACS Catal. 2017, 7, 4423−4434

transferred into the spectrometer for analysis. The spectra were collected using 3 keV He^+ at 2×10^{14} ions cm^{-2} or 5 keV Ne^+ at 1×10^{14} ions cm^{-2} as ion sources. For depth profiling, the surface was sputtered with 0.5 keV Ar^+ at 5×10^{14} cm^{-2} per profile cycle, corresponding to approximately 0.1 nm.

2.3. Steady State Kinetic Measurement. The conversion of 2-propanol was performed in an Altamira Instruments system (AMI-200). Each catalyst sample (30 mg, sieved to 63−125 μm) was diluted with quartz sand (177−250 μm) to minimize channeling and local temperature differences. The quartz-to-catalyst mass ratio was approximately 12:1. The catalyst bed was placed inside a quartz u-tube and held in place by quartz wool at both ends of the bed. Each sample was pretreated under 50 mL/min of 5% O_2 in Ar or He at approximately 550 °C for 1 h. The temperature was lowered to around 300 °C, and the gas was switched to 50 mL/min of Ar. Liquid 2-propanol was fed into the system using a Chemyx Nexus 3000 syringe pump. All experiments were performed under conditions free of mass transfer limitations (see Supporting Information including Figures S1 and S2, and Tables S1 and S2). Products were analyzed using a Buck Scientific Model 910 gas chromatograph (GC) equipped with a flame ionization detector and a Restek MXT-Q-BOND column. The GC response factor was calibrated employing 2-propanol as an internal standard and assuming a closed mass balance in the system. All lines were heated to avoid condensation. Each experiment was performed under differential conditions (conversion less than 13%) to determine activation energies. Thus, any effects of concentration and temperature gradients throughout the catalyst bed were minimized.

2.4. Adsorption and Temperature-Programmed Desorption of 2-Propanol Followed by FTIR Spectroscopy. The adsorption of 2-propanol was performed using the Thermo Nicolet Nexus 670 FTIR spectrometer described in the above section. The sample was activated in a diffuse reflectance cell (Pike Technologies HC-900) at 550 °C for 1 h under 30 mL/min of 5% O_2/He before the gas flow was switched to 30 mL/min of He, and background spectra were taken at 300, 200, 100, and 25 °C during the cooling process in flowing He. He was bubbled through a saturator filled with liquid 2-propanol at 25 °C. A pulse of 2-propanol saturated gas (sample loop 0.5 mL) was introduced into the sample cell, purged with He for 10 min, and a spectrum was taken. The sample was heated to 100, 200, and 300 °C, and a spectrum was taken at each temperature.

2.5. Adsorption Microcalorimetry of 2-Propanol and Acetone. Adsorption microcalorimetry experiments were performed using a Micromeritics 3Flex Characterization analyzer coupled with a Setaram Sensys Evo DSC microcalorimeter as described above. Each sample was evacuated and activated at 550 °C for 1 h, dosed with 500 mmHg of O_2, evacuated for 30 min each for two rounds, and cooled down to 30 °C. The temperature was held for 1 h to reach thermal equilibrium, and the sample was exposed to doses of 2-propanol or acetone. Prior to adsorption, the 2-propanol and acetone used in the experiments were degassed by three cycles of freeze−pump−thaw in a stainless-steel reservoir.

2.6. DFT Calculations. All periodic density functional theory (DFT) calculations were performed with the Vienna ab initio Simulation Package (VASP).[31,32] The Perdew−Burke−Ernzerhof (PBE)[33] functional of generalized-gradient approximation (GGA) was used for electron exchange and correlation. The electron−core interaction was described using the projector-augmented wave method (PAW).[34,35] A kinetic energy cutoff of 450 eV was used for the planewave basis set, and the Brillouin zone was sampled using a 3 × 3 × 1 Monkhorst−Pack scheme.[36] The adsorption energies were calculated using the definition $E_{ads} = E_{surface+adsorbate} - (E_{surface} + E_{adsorbate})$, where the energy of the adsorbate $E_{adsorbate}$ was computed by placing the adsorbate in a 15 Å wide vacuum cubic cell. The surface slabs of the studied ABO_3 perovskites were created containing three AO layers and three BO_2 layers, for a total of six, with a 15 Å vacuum layer. A 2 × 2 supercell of the slabs was created from the unit cell. 2-Propanol adsorption on the perovskites and the active site displacement calculations were obtained where the top two layers of the slabs were allowed to relax. This is compared to the adsorption of 2-propanol for which the surface atoms are kept fixed, and the propanol is situated over the same site to study the effect of site displacement on adsorption energy.

3. RESULTS

3.1. Catalyst Properties and Surface Density of Acid−Base Sites. Table 1 shows the tolerance factor and physical properties derived from nitrogen physisorption of the perovskite catalysts. The tolerance factor was calculated using the ionic radii obtained from the literature.[3] $SrTiO_3$, $BaTiO_3$, $SrZrO_3$, and $BaZrO_3$ have a tolerance factor ranging from 0.83 to 1.04, indicating that the crystal structure of each perovskite is expected to be stable. The measured surface area and pore volume of $SrTiO_3$ are the highest, while they are similar for the other three perovskites.

Table 1. Tolerance Factor and Physical Properties Derived from Nitrogen Physisorption of Perovskite Catalysts

catalyst	tolerance factor[a]	surface area (m^2/g)	pore volume (cm^3/g)
$SrTiO_3$	0.91	24	0.106
$BaTiO_3$	1.04	6	0.007
$SrZrO_3$	0.83	7	0.017
$BaZrO_3$	0.91	8	0.010

[a]Calculated from the literature.[3]

Figure 1 shows the XRD patterns of the four stable perovskite catalysts. The XRD pattern of $SrTiO_3$ contains major peaks at 32.7°, 40.3°, 46.7°, 58.1°, and 68.2°. These are attributed to the (110), (111), (200), (211), and (220) planes of its cubic crystal structure, respectively.[37,38] In the case of cubic $BaTiO_3$, these peaks are observed at about 1° lower compared to those for $SrTiO_3$,[39,40] indicating an increase in the

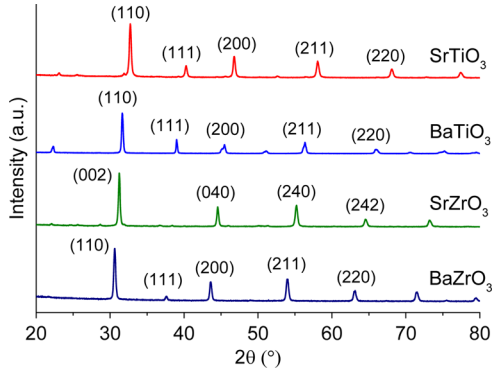

Figure 1. XRD patterns of perovskite catalysts.

DOI: 10.1021/acscatal.7b00783
ACS Catal. 2017, 7, 4423−4434

lattice parameter. In the case of $BaZrO_3$, the peaks at 30.6°, 37.7°, 43.6°, 54°, and 63.1° correspond to the (110), (111), (200), (211), and (220) planes of its cubic phase, respectively.[41,42] For $SrZrO_3$, the perovskite with the smallest tolerance factor, characteristic peaks of its orthorhombic crystal structure are observed at 31.3°, 44.5°, 55.2°, and 64.6°, which are assigned as (002), (040), (240), and (242) planes, respectively.[43,44] Figure S3 in the Supporting Information shows the SEM images of the perovskite catalysts. $SrTiO_3$ displayed the smallest crystallite size of less than 100 nm, while $BaTiO_3$ showed the largest crystallite size of around 500 nm. $SrZrO_3$ and $BaZrO_3$ have an average crystallite size of ~400 nm.

Low energy ion scattering (LEIS) was performed to analyze the composition at the top surface of the perovskite catalysts, as it was shown that LEIS is particularly suited to determine the composition of the top atomic monolayer of material (~0.3 nm) with a sensitivity on the order of 0.1 atomic %.[29,30] Figure 2 shows the ratio of the integrated scattering intensity of the A

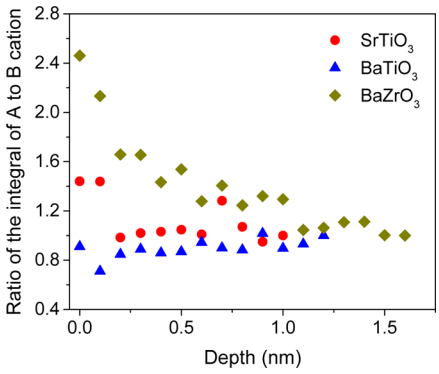

Figure 2. Surface A/B cation intensity ratio of the four perovskite catalysts as a function of probing depth using low energy ion scattering (LEIS).

to B cation as a function of depth. The ratios are normalized to unity at the greatest depth for each sample. Because of the small difference in mass between Sr and Zr, the peaks for $SrZrO_3$ could not be resolved. For $SrTiO_3$ and $BaZrO_3$, there is evidence of enrichment of the A cation at the surface but not for $BaTiO_3$.

Microcalorimetry was used to probe the concentration and strength of acid and base sites on the perovskite samples. The heats of adsorption of NH_3 and CO_2 were measured as a function of surface coverage, and the results are shown in Figure 3. $SrTiO_3$ displayed the highest initial differential heat of NH_3 adsorption, followed by $BaTiO_3$ (Figure 3A). $SrZrO_3$ and $BaZrO_3$ have a similar initial heat of adsorption around 53 kJ/mol. The differential heat of NH_3 adsorption on $SrTiO_3$ remained constant up to a surface coverage of 0.43 μmol/m^2 and decreased at higher surface coverage. For the remaining three perovskites, the differential heat of NH_3 adsorption decreased as a function of surface coverage, reaching values between 20 and 40 kJ/mol. This suggests the physisorption of NH_3 at higher surface coverage.[45,46]

The initial heats of adsorption of CO_2 are similar between $SrZrO_3$ and $BaZrO_3$ at ~125 kJ/mol, which were around 20 kJ/mol higher compared to those of $SrTiO_3$ and $BaTiO_3$ (Figure 3B). Up to a surface coverage of 2.4 μmol/m^2, the heat of adsorption of CO_2 on $SrTiO_3$ remained constant around 105 kJ/mol, and it gradually decreased. For the other three

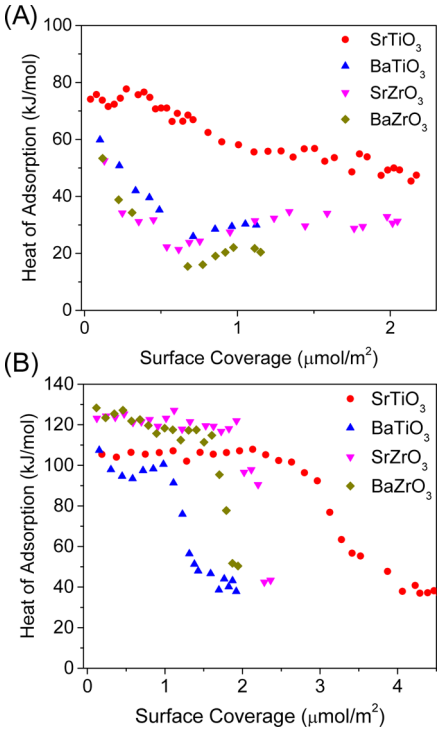

Figure 3. Heat of adsorption of (A) NH_3 and (B) CO_2 on perovskite catalysts measured at 150 and 30 °C, respectively.

perovskites, the differential heats of CO_2 adsorption decreased slightly as a function of surface coverage, followed by a sharp drop at various surface coverages.

Table 2 shows the surface density of acid and base sites on the perovskite catalysts, which was determined by the

Table 2. Surface Density of Acid and Base Sites on Perovskite Catalysts

catalyst	acid site (μmol/m^2)	base site (μmol/m^2)	ratio of base to acid site
$SrTiO_3$	0.42	3.47	8.26
$BaTiO_3$	0.29	1.25	4.31
$SrZrO_3$	0.35	2.78	7.94
$BaZrO_3$	0.26	2.11	8.12

concentration of irreversibly adsorbed NH_3 and CO_2, respectively. $SrTiO_3$ has the highest surface density of the acid site, followed by $SrZrO_3$. $BaTiO_3$ and $BaZrO_3$ have similar surface densities of acid sites. For the base site, $SrTiO_3$ also has the highest surface density, followed by $SrZrO_3$, $BaZrO_3$, and $BaTiO_3$. The surface density of base sites in Table 2 is higher than the surface density of base sites at constant heat of adsorption (Figure 3), indicating that the adsorption of CO_2 with a lower differential heat of adsorption is also irreversibly adsorbed. In terms of the ratio of base to acid site, $SrTiO_3$, $SrZrO_3$, and $BaZrO_3$ have similar values, while the ratio for $BaTiO_3$ is approximately half compared to that of the other perovskites. Overall, all of the perovskite surfaces are dominated with basic sites.

Pyridine and CO_2 adsorption followed by in situ FTIR spectroscopy were performed to investigate the nature of the acid and base sites of the perovskite catalysts, respectively. The FTIR spectra for the adsorption of pyridine on the perovskites showed two main peaks around 1595 and 1443 cm^{-1} (Figure

DOI: 10.1021/acscatal.7b00783
ACS Catal. 2017, 7, 4423−4434

S4A). These peaks are assigned as pyridine coordinatively adsorbed to the Lewis acid site.[47,48] In general, for the peak around 1595 cm^{-1}, it increases in wavenumber as the strength of Lewis acid site increases. In the case of η-Al_2O_3, weak, medium, and strong Lewis acid sites were observed at 1595, 1613, and 1623 cm^{-1}, respectively.[49] Thus, most of the Lewis acid sites on the perovskite catalysts are weakly acidic, while the shoulders around 1618 cm^{-1} indicate a small concentration of Lewis acid sites with medium strength. The absence of a peak at 1540 cm^{-1} indicates that no apparent Brønsted acid sites are present on these perovskite catalysts.

The FTIR spectra for the adsorption of CO_2 on the perovskites are shown in Figure S4B. The formation of both bidentate and unidentate carbonates are observed on the perovskite catalysts, indicating that basic surface oxygen atoms are exposed on the surface.[50−52] The absence of bicarbonate species implies that basic surface hydroxyl groups are not present on these perovskites. Table S3 summarizes the peak assignments of the observed carbonates formed from CO_2 adsorption.

To estimate the ratio of acid and base sites that are still in equilibrium with the titrants at the reaction temperature of 300 °C for 2-propanol conversion (see below), the integral of the peaks in the FTIR spectra for the adsorption of pyridine or CO_2 was obtained at the adsorption temperature (I_{ads}) and 300 °C (I_{300}). For pyridine adsorption, the integral of the peak around 1595 cm^{-1} was used. For CO_2 adsorption, the integral of the peaks between 1800 to 1200 cm^{-1} was used. The ratio of the integral (I_{300}/I_{ads}) gives an estimation of the titrants that are still adsorbed at 300 °C, and the result is shown in Table 3. At the reaction temperature of 300 °C, the surface coverage of acid and base sites decreased significantly.

Table 3. Percentage of Acid and Base Sites in Equilibrium with Titrants at a Reaction Temperature of 300 °C Based on the Ratio (I_{300}/I_{ads}) of the FTIR Peak Integral of Pyridine and CO_2 Adsorption between 300 °C and Adsorption Temperature (Pyridine, 150 °C; CO_2, 25 °C)

	acid site (%)	base site (%)
$SrTiO_3$	31	24
$BaTiO_3$	80	39
$SrZrO_3$	62	25
$BaZrO_3$	41	51

3.2. Steady State Kinetic Measurement of 2-Propanol over Perovskite Catalysts. Conversion of 2-propanol over the four perovskite catalysts was performed in the temperature range of 286−320 °C under differential conditions (conversion less than 13%). The Arrhenius plots are shown in Figure 4, and the apparent activation energies for dehydration and dehydrogenation reactions are summarized in Table 4. Propene and acetone are the only products observed with acetone as the major product (Figure 5). The selectivity to acetone is higher than 70% for each perovskite. $BaTiO_3$ showed the highest apparent activation energy for dehydration and dehydrogenation, while $SrZrO_3$ showed the lowest apparent activation energy for both reactions. Between 280 and 320 °C, the selectivity toward acetone production increased with temperature, except for $SrZrO_3$ (Figure 5).

3.3. Adsorption and Temperature-Programmed Reaction of 2-Propanol Followed by FTIR Spectroscopy. Figure 6 shows the FTIR spectra of 2-propanol adsorbed on the

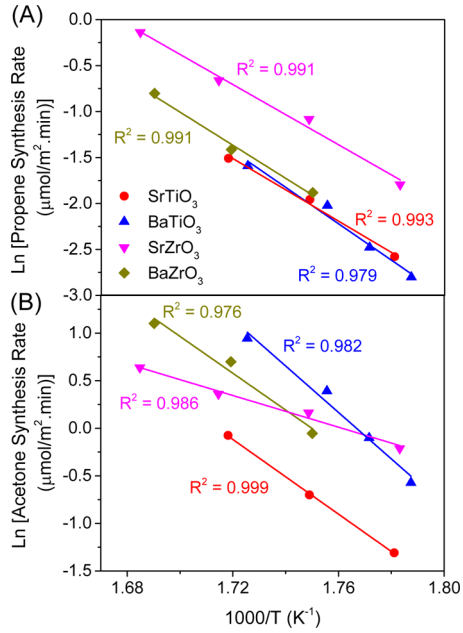

Figure 4. Arrhenius plots for the production of (A) propene and (B) acetone from 2-propanol over perovskite catalysts. Reaction conditions: 286−320 °C and 50 mL/min Ar. WHSV: 0.8 h^{-1}.

Table 4. Apparent Activation Energies for Dehydration and Dehydrogenation of 2-Propanol over Perovskite Catalysts[a]

	apparent activation energy (kJ/mol)	
catalyst	dehydration	dehydrogenation
$SrTiO_3$	141	163
$BaTiO_3$	164	203
$SrZrO_3$	136	69
$BaZrO_3$	150	161

[a]Reaction conditions: 286−320 °C and 50 mL/min Ar. WHSV: 0.8 h^{-1}.

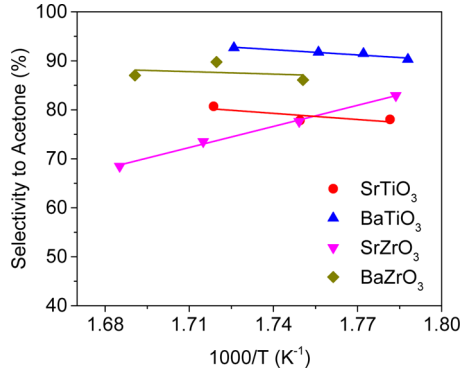

Figure 5. Selectivity toward acetone for the conversion of 2-propanol over perovskite catalysts. Reaction conditions: 286−320 °C and 50 mL/min Ar. WHSV: 0.8 h^{-1}.

perovskites. For pure liquid 2-propanol, the two peaks at 1381 and 1369 cm^{-1} are assigned as the symmetric δCH_3 vibration, while the peaks at 1342 and 1313 cm^{-1} are attributed to δCH and δOH vibration, respectively.[53−56] Peaks observed at 1164, 1132, and 1113 cm^{-1} are related to νC−C, ρCH_3, and νC−O vibrations, respectively.[57] Several changes are observed when 2-propanol is adsorbed on the perovskite catalysts at 25 °C. Table 5 summarizes the peak assignments. The most prominent

DOI: 10.1021/acscatal.7b00783
ACS Catal. 2017, 7, 4423−4434

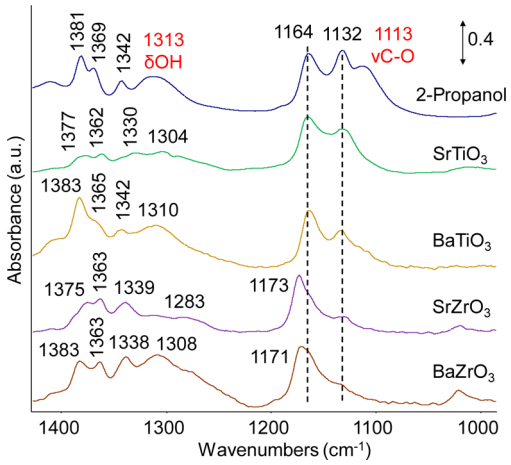

Figure 6. FTIR spectra of 2-propanol adsorption on perovskite catalysts at 25 °C.

Table 5. Peak Assignment of 2-Propanol Adsorption and Temperature-Programmed Reaction on Perovskite Catalysts

frequency (cm^{-1})	assignment	group
1693	νC═O	acetone
1578	νC═C	propene
1470	$\delta_{asym}CH_3$	2-propanol
1389−1362	$\delta_{sym}CH_3$	
1342−1330	δCH	
1329−1283	δOH	
1173−1164	νC−C and νC−O	
1132	ρCH_3	

change is that the peak at 1113 cm^{-1} (νC−O) vanished. In addition, the relative intensity of the peak at 1164 cm^{-1} to that of 1132 cm^{-1} for $SrTiO_3$ and $BaTiO_3$ increased, suggesting that the peak due to νC−O vibration shifted to higher wavenumbers and possibly overlapped with the peak at 1164 cm^{-1}. For $SrZrO_3$ and $BaZrO_3$, the peak at 1164 cm^{-1} blue-shifted to around 1172 cm^{-1}, suggesting that the peak due to νC−O shifted even further. This indicates that the oxygen atom of 2-propanol is interacting with the surface of the zirconate perovskites to a different extent, which is also supported by the red shift of the peak due to δOH vibration. The largest shift was observed for $SrZrO_3$.

After the adsorption of 2-propanol at 25 °C, the temperature was increased under flowing He to observe its reaction on the surface. Only the FTIR spectra for the temperature-programmed reaction of 2-propanol on $BaTiO_3$ is shown in Figure 7, as the results are similar for the rest of the perovskites (Figure S5). At room temperature, a negative peak is observed at 1640 cm^{-1}, which could be attributed to the displacement of water molecules.[57] As the temperature increased from 25 to 100 °C, the relative intensity of the peak at 1310 cm^{-1} (δOH) decreased slightly, suggesting the dissociation of the alcohol group. By 200 °C, the intensity of the peaks due to adsorbed 2-propanol decreased, while two new peaks are observed at 1693 and 1578 cm^{-1}. These two peaks are due to the νC═O and νC═C vibrations of acetone and propene, respectively,[57] indicating the occurrence of surface conversion of adsorbed 2-propanol. At 300 °C, the peak due to acetone has vanished, probably due to the desorption of the adsorbed acetone species.

3.4. Adsorption Microcalorimetry of 2-Propanol and Acetone. Figure 8 shows the differential heats of 2-propanol

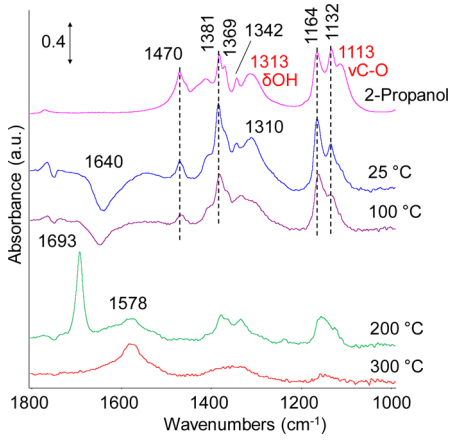

Figure 7. FTIR spectra of temperature-programmed reaction of 2-propanol on $BaTiO_3$.

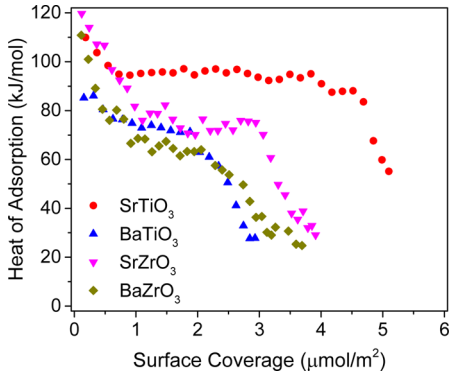

Figure 8. Heat of adsorption of 2-propanol on perovskite catalysts measured at 30 °C.

adsorption on the perovskite catalysts at 30 °C. $SrZrO_3$ displayed the highest initial heat of adsorption of 120 kJ/mol, while $BaTiO_3$ showed the lowest initial heat of adsorption of 85 kJ/mol. $SrTiO_3$ and $BaZrO_3$ have similar intermediate values. Differential heat of adsorption generally decreased as a function of surface coverage. In the case of $SrTiO_3$, the heat of adsorption decreased to 95 kJ/mol and remained constant up to a surface coverage of 4 μmol/m^2, followed by a decrease again.

The heat of adsorption of acetone on the perovskite catalysts was also measured as acetone is a major product in the conversion of 2-propanol. The initial heat of adsorption of acetone ranges between 90 and 120 kJ/mol (Figure S6) over the four perovskites. As surface coverage increased, the differential heat of acetone adsorption on the perovskites decreased gradually.

3.5. Density Functional Theory Calculations of Adsorption Geometry and Energetics. To provide atomistic insights into the adsorption and surface chemistry of 2-propanol on the perovskite catalysts, we examined both A- and B-terminated surfaces with the low-Miller-index (001) facet. Experimentally, the (001) facet is predominantly exposed,[58−61] consistent with theoretical studies of surface energy showing the (001) facet to be the most stable for this class of perovskites.[62,63] Figure 9 shows the final adsorption configuration of 2-propanol on $BaTiO_3$ from DFT calculations, which is representative of the other perovskites. On the A-cation-terminated surface, the hydrogen atom from the alcohol group

DOI: 10.1021/acscatal.7b00783
ACS Catal. 2017, 7, 4423−4434

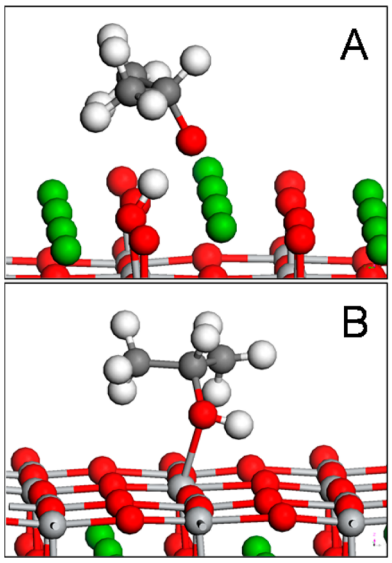

Figure 9. Adsorption configuration of 2-propanol on $BaTiO_3$ (001) for (A) Ba^{2+} or the A-cation-terminated surface and (B) Ti^{4+} or the B-cation-terminated surface from DFT geometry optimization. Red, oxygen; green, Ba; light gray, Ti; dark gray, C; white, H.

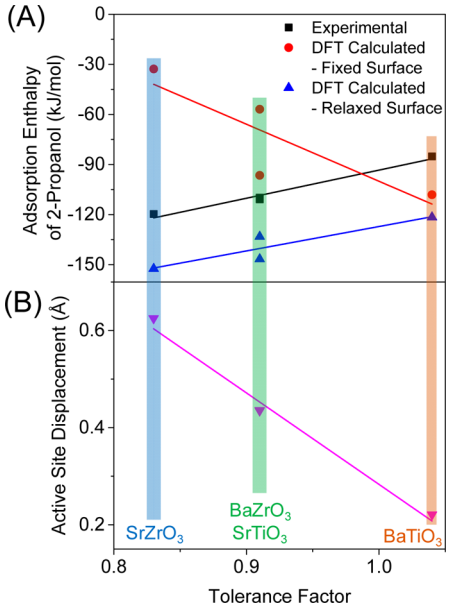

Figure 10. (A) Correlation of the adsorption energy of 2-propanol with the tolerance factor of the bulk perovskites for experimental adsorption energy, DFT-computed adsorption energy on a relaxed A surface, and DFT-computed adsorption energy on an unrelaxed (or fixed) A surface. (B) Correlation of active site displacement on the A-terminated surface (that is, oxygen atom relaxation from DFT geometry optimization) with the tolerance factor.

of 2-propanol dissociated spontaneously and formed a hydroxyl group with a surface oxygen atom (O*), while the oxygen atom of 2-propoxide interacts with the hydroxyl group (Figure 9A). The distance between the dissociated O and H atom is calculated to be around 1.47 Å, while the length of the O*−H bond is approximately 1.04 Å (Table S4). For the B-cation-terminated surface, the oxygen atom from the alcohol group of 2-propanol interacts with the surface B cation (B*), resulting in a Lewis acid−base interaction. The length of the alcohol O−H bond is approximately 0.98 Å, while the length of the O−B* bond is around 2.2 Å. As listed in Table S4, the calculated adsorption energy of 2-propanol on the A-cation-terminated surface is consistently higher than on the B-terminated surface for the perovskites, except for $BaTiO_3$. Figure S7 shows a positive correlation between the experimental and average DFT adsorption energies of 2-propanol on the perovskite catalysts. The average DFT adsorption energy was calculated using the surface density of acid and base sites obtained in Table 2, assuming that the A- and B-terminated surfaces are responsible for the base and acid sites, respectively. The trend shows that $SrZrO_3$ displayed the highest adsorption energy for 2-propanol, followed by $BaZrO_3$, $SrTiO_3$, and $BaTiO_3$.

Figure 10A shows the adsorption energy of 2-propanol on the A-cation-terminated perovskites obtained using DFT calculation compared to values obtained using the micro-calorimeter. For theoretical calculations, the adsorption energy of 2-propanol was shown for both fixed (i.e., ideally truncated and unrelaxed; see result in Table S4) and relaxed surfaces. For a fixed surface, the adsorption energy decreases with increasing tolerance factor. However, when the A-cation-terminated surface is allowed to relax, the resulting adsorption energy increases linearly with the tolerance factor, which is similar to the trend observed for experimental values. This indicates that the more cubic the perovskite (tolerance factor closer to 1), the lower is the surface relaxation after 2-propanol adsorption and the lower is the adsorption strength. After the surface is allowed to relax, the surface oxygen atom is displaced to a certain extent as it interacts with the hydrogen atom of the alcohol group. We call this relaxation of the surface oxygen atom the active site displacement. Figure 10B shows a negative correlation between the active site displacement and the tolerance factor of the perovskite catalysts. $BaTiO_3$ displayed the highest tolerance factor and the least active site displacement, while $SrZrO_3$ exhibited the highest displacement of the surface oxygen atom. $SrTiO_3$ and $BaZrO_3$ have similar values. The displacement of active site on the B-cation-terminated surface is negligible.

3.6. Correlation between Acetone Synthesis Rate and Surface Heat of Reaction. Scheme 1 shows a simplified potential energy diagram on the dehydrogenation of 2-propanol to acetone. Briefly, gaseous 2-propanol chemisorbs to the surface, forms a transition state, undergoes dehydrogenation to form adsorbed acetone and hydrogen, and the products desorb as gas phase species. It is assumed that molecular hydrogen physisorbs to the surface of the perovskite catalysts under steady state reaction condition since the enthalpy of adsorption ($\Delta H_{ads,hydrogen}$) from our DFT calculation is shown to be small for the perovskite catalysts (Table S5). Another assumption is

Scheme 1. Potential Energy Diagram on the Dehydrogenation of 2-Propanol to Acetone

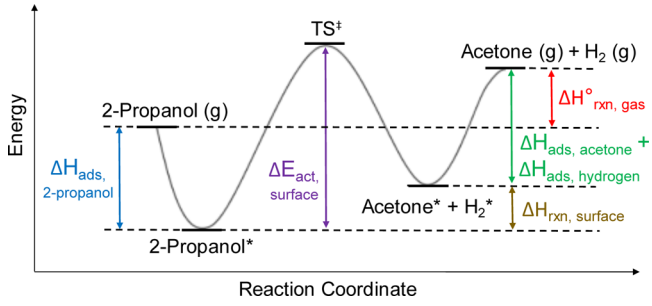

DOI: 10.1021/acscatal.7b00783
ACS Catal. 2017, 7, 4423−4434

that the activation energy for the dissociation of the hydrogen atom on the alcohol group of 2-propanol is negligible (vide infra). Hence, the removal of hydrogen atoms from adsorbed 2-propanol to form acetone can be considered as a single elementary step. On the basis of Scheme 1, the surface heat of reaction ($\Delta\hat{H}_{rxn,surface}$) can be approximated using the following equation (see the detailed derivation in Supporting Information).

$$\Delta\hat{H}_{rxn,surface} \approx -\Delta H_{ads,\ acetone} + \Delta H_{ads,2\text{-}propanol}$$

where $\Delta H_{ads,acetone}$ and $\Delta H_{ads,2\text{-}propanol}$ are the adsorption energy of acetone and 2-propanol, respectively.

The adsorption energy of 2-propanol and acetone is obtained using the initial heat of adsorption measured from microcalorimetry (Figures 8 and S6). Although there is a distribution of adsorption sites as evidenced by adsorption microcalorimetry at lower temperatures, only the initial adsorption energies of 2-propanol and acetone are used to estimate $\Delta\hat{H}_{rxn,surface}$ (vide infra).

Figure 11 shows that there is a negative correlation between acetone synthesis rate and $\Delta\hat{H}_{rxn,surface}$ for $SrTiO_3$, $BaTiO_3$, and $BaZrO_3$ between 290 to 310 °C. $SrZrO_3$ is not shown as the rate of acetone synthesis does not fit the trends due to its orthorhombic crystal structure, as discussed below. At all temperatures, $BaTiO_3$ displayed the highest acetone synthesis rate and lowest $\Delta\hat{H}_{rxn,surface}$, followed by $BaZrO_3$ and $SrTiO_3$.

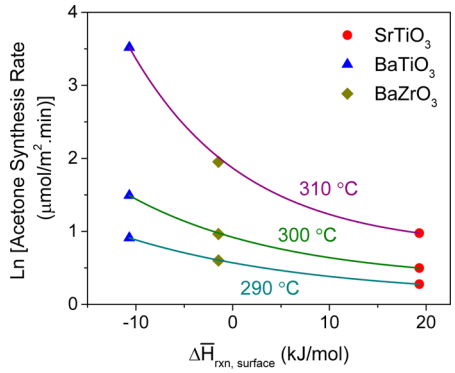

Figure 11. Correlation between acetone synthesis rate and surface heat of reaction over three perovskites.

4. DISCUSSION

4.1. Dependence of Acid–Base Sites on the Surface Composition of Perovskites. Acid–base properties are key parameters in oxide catalysts to determine the selectivity and activity of catalytic reactions. Furthermore, the surface structure of metal oxides is a major factor that dictates the nature of surface acid and base sites where acid–base reactions essentially take place. Thus, it is important to elucidate the composition of the top surface and correlate it to its surface properties, especially for binary oxides such as perovskites. In this way, the acid–base properties of metal oxides can be tuned by modulating its surface composition. However, there are very limited reports in the literature related to the dependence of acid–base sites on surface termination of perovskites. Tesquet et al. synthesized various $LaFeO_3$ perovskites with increasing La content and evaluated their acid–base properties from the reactivity of 2-propanol.[64] Excess lanthanum in the perovskite resulted in surface enrichment of La_2O_3, and the selectivity to acetone increased with higher La content. However, the surface composition of $LaFeO_3$ without excess La was not reported. Sahu et al. measured the formation enthalpy and surface energetics of various niobate and tantalate perovskites.[65] The authors correlated the stability of perovskites with their acid–base chemistry without further characterization.

In this study, on the basis of LEIS analysis, it is shown that $SrTiO_3$ and $BaZrO_3$ have a higher ratio of A to B cation on the surface, while this ratio is close to 1 for $BaTiO_3$ (Figure 2). In comparison to its surface properties, the ratio of base to acid sites on $SrTiO_3$ and $BaZrO_3$ is around two times that on $BaTiO_3$ (Table 2). This suggests that the higher ratio of A cations on the surface of perovskites resulted in a higher surface density of base sites, which are basic surface oxygen atoms (Table S3). Since the ratio of base to acid sites on $SrZrO_3$ is relatively high, it is conceivable that this perovskite also has a higher ratio of Sr to Zr on the surface, although LEIS analysis cannot differentiate between Sr and Zr. Furthermore, most of the Lewis acid sites on the perovskite catalysts are weak, while there are intermediate and strong basic surface oxygen atoms (Figure S4).

Figure 3 shows that the Lewis acid sites of titanates are stronger than those of zirconates, while the basic surface oxygen atoms of zirconates are stronger than those of titanates. The decreasing trend of the heat of adsorption of NH_3 on $BaTiO_3$, $SrZrO_3$, and $BaZrO_3$ reflects the heterogeneity of the surface acid sites, whereas the constant heat of adsorption with coverage on $SrTiO_3$ suggests that the distribution of acid sites is more homogeneous. For the adsorption of CO_2, the difference in the distribution of base sites on the perovskites is likely due to the different ratios of A to B cations on the surface as evidenced by LEIS analysis (Figure 2), as perovskites enriched with A cations have a higher surface density of base sites. It has been shown in the literature that TiO_2 has stronger Lewis acid sites compared to those of ZrO_2,[51] indicating that the Lewis acid sites on the perovskite catalysts are due to the unsaturated surface B cations. However, although BaO has stronger base sites compared to those of SrO,[66] the surface basicity is similar for the two titanates or zirconates, with the two zirconates being more basic. Thus, although the acid–base properties of perovskites are a result of the interplay between the A and B cations exposed on the surface, it appears that the strength of both the acid and the base sites is more affected by the type of B cation on the surface.

The higher ratio of A cations and the strong basicity on the surface of the perovskites suggest that the crystal structure is largely terminated by SrO or BaO, which are basic in nature.[66] In contrast, surface studies on similar perovskites in the literature reported that the surface is mainly terminated by BO_x. Erdman et al. used high resolution electron microscopy and density functional theory to study the surface termination of single crystal $SrTiO_3$ (001) surfaces.[60,67] It was reported that the crystal is terminated by TiO_x polyhedrons and that the structure formation rule can be extended to other perovskites. Computational studies on the surface structure of $BaTiO_3$ and $SrZrO_3$ concluded that the BO_x-terminated surface appears to be more stable,[68,69] while the surface energies of BaO and ZrO_2 are similar for $BaZrO_3$.[70] However, the effect of high temperature pretreatment in the presence of oxygen was not taken into account in the literature, which could explain the difference in surface termination observed in this study. Recently, Dagdeviren et al. reported that high temperature treatment under oxygen atmosphere or ultrahigh vacuum

DOI: 10.1021/acscatal.7b00783
ACS Catal. 2017, 7, 4423–4434

(UHV) alters the surface structure of the $SrTiO_3$ (100) single crystal and the ratio of A to B cations.[71] Hence, the results reported here suggest that the surface of these perovskites is largely terminated by SrO or BaO under reaction conditions. It remains an interesting area to investigate the surface composition of perovskites under different treatments and even reaction conditions.

4.2. Adsorption of 2-Propanol and Its Dependence on Tolerance Factor. The adsorption of 2-propanol has been extensively studied over various oxide catalysts. These catalysts include MgO,[54] NiO,[72] layered double hydroxide containing Mg and Al,[53] and common metal oxides such as Al_2O_3, TiO_2, SiO_2, and Nb_2O_5.[23,56] In most of these studies, on the basis of the disappearance of the δOH vibrational peak, it was reported that 2-propanol adsorbs dissociatively on metal oxides. To our knowledge, there have been no reports on the adsorption of 2-propanol on perovskites. Understanding the adsorption and conversion of 2-propanol on perovskite catalysts will help to elucidate the role of acid and base sites in the reaction mechanism.

In this study, the existence of the δOH IR peak (Figure 6) indicates the presence of undissociated 2-propanol adsorbed on the four perovskite catalysts at 25 °C. However, the presence of dissociated 2-propanol can also be inferred on the perovskites enriched with A cations, as DFT calculations have shown that 2-propanol adsorbs dissociatively on an A-cation-terminated surface (Figure 9A). Furthermore, the decrease in relative intensity of the δOH vibrational peak at 100 °C indicates the dissociation of the alcohol group, while both the frequency and intensity of the νC−O vibrational mode remain unchanged (Figure 7). This suggests that the νC−O vibrational mode of dissociated 2-propanol on the surface is very similar in frequency to that of the undissociated species, such that the additional dissociation at 100 °C does not result in intensity change of the νC−O mode. Therefore, both undissociated and dissociated 2-propanol are present on the perovskite surfaces upon room temperature adsorption, and only dissociated 2-propanol is present at higher temperatures.

The frequency of the νC−O vibration blue-shifted further for zirconates compared to that for titanates, indicating that the oxygen atom of the alcohol group is involved in surface interaction to a larger extent. In addition, the experimental results are in good agreement with DFT calculations, which shows that the adsorption energy on an A-cation-terminated surface for $AZrO_3$ is higher in magnitude compared to that of $ATiO_3$ (Table S4).

Copeland et al. studied the adsorption of glycerol on various metal oxides such as Al_2O_3, CeO_2, MgO, TiO_2, and ZrO_2 and reported a positive linear correlation between the frequency of νC−O vibration and the electronegativity of the metal atom.[51] It was suggested that the increasing electronegativity of the metal cation can draw electron density from the oxygen atom. Subsequently, the oxygen atom draws electron density from the carbon atom to a smaller extent, resulting in increased dipole between the alkoxy carbon and oxygen atom. As such, surface interaction with the alcohol group would shift the νC−O vibrational frequency to higher wavenumbers, which was observed for the adsorption of 2-propanol (Figure 6). In the case of the perovskites studied here, the frequency for the νC−O vibration is higher for zirconates compared to that for titanates. However, the electronegativity for a Zr cation is lower compared to that of a Ti cation.[48] We believe this positive linear correlation cannot be applied to mixed oxides such as perovskites because the surface of the four perovskites is terminated with a mixture of BO with a larger proportion of AO (vide supra). Thus, the measured Lewis acidity of the perovskites could be influenced by the presence of the A cations exposed on the surface in addition to the B cations.

Comparison between the relaxed vs unrelaxed surfaces (Figure 10A) suggests that the DFT-computed adsorption energy of the reactant (2-propanol) is not only related to the chemical identity of the surface cations but that it is largely presided over by the tolerance factor (a bulk property) of the perovskites, which describes the relative size of the cations in the structure. Perovskites with a tolerance factor deviating from unity tend to displace its active site proportionally to stabilize the adsorbate, leading to stronger adsorption. Although $SrZrO_3$ has a different crystal structure and surface geometry, the adsorption enthalpy of 2-propanol is still linearly correlated with the tolerance factor. This suggests that $\Delta H_{ads,2\text{-}propanol}$ encompasses the change in surface geometry related to the bulk structure, and the synergy between acid and base site, as the adsorption and dissociation of 2-propanol occurs on both types of surface sites as discussed below.

4.3. Reaction Mechanism of 2-Propanol on Perovskite Catalysts. The reaction mechanism of 2-propanol conversion over the four perovskites can be deduced from the results of the surface chemistry of 2-propanol and the properties of the acid and base site. Several reaction mechanisms have been proposed in the literature for the formation of acetone and propene from 2-propanol over oxide surfaces. In general, the dehydration of alcohols can occur via three different mechanisms, E_1, E_2, and E_{1cB}.[22,52,73−75] The E_1 mechanism is a two-step pathway catalyzed only by strong acid sites, where a carbenium ion is formed from the release of an OH^- group, followed by the loss of a H^β proton. This mechanism can be excluded for the perovskites as most of the Lewis acid sites on the perovskites are weakly acidic as indicated by the IR-pyridine adsorption study. The second pathway is the E_2 elimination mechanism, which occurs in a single step on an acid−base pair of intermediate strength. In this pathway, the OH group and the H^β proton are removed in a concerted mechanism. Similarly, this is not likely for the perovskites due to the weak acidity of the surface sites. The E_{1cB} pathway, which is accompanied by the dehydrogenation reaction, is a two-step pathway involving weak Lewis acid and strong base sites (Scheme 2), similar to the surfaces of the perovskites studied here. As such, the E_{1cB} mechanism is the most likely pathway for 2-propanol conversion over our perovskite catalysts. The alcohol group of 2-propanol is initially deprotonated by a basic surface oxygen atom, forming a surface OH group, while the alkoxide is adsorbed on an adjacent Lewis acid site. Results from FTIR spectroscopy support the presence of 2-propoxide as the reaction intermediate (Figures 6 and 7). Subsequently, the abstraction of H^α or H^β would lead to the formation of acetone or propene, respectively. It has been suggested that the selectivity to acetone or propene would depend on the relative acidity of H^α or H^β and the basic properties of the acid−base sites.[75] Since both acid and base sites are required for dehydration and dehydrogenation, it is proposed that a balance or synergism between the acid and base sites on the perovskite surface determines the product selectivity or the rate of acetone and propene production in the conversion of 2-propanol. This kind of synergism between acid and base sites for alcohol conversion was also observed over other metal oxides.[76−79]

DOI: 10.1021/acscatal.7b00783
ACS Catal. 2017, 7, 4423−4434

Scheme 2. Proposed E_{1cB} Mechanism for the Dehydration and Dehydrogenation of 2-Propanol over Perovskite Catalysts

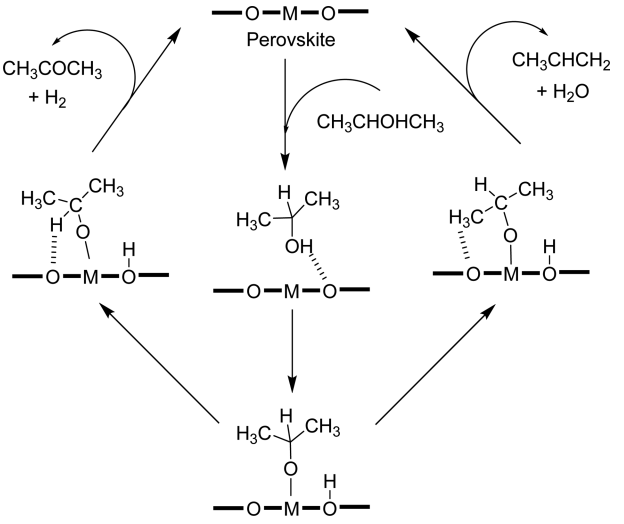

The E_{1cB} mechanism over the perovskite surfaces is further supported by our DFT results. DFT calculations show that 2-propanol has a different adsorption configuration on different surface terminations (Figure 9) of the perovskites. On an A-cation-terminated surface, the hydrogen atom of the alcohol group is dissociated and forms a hydroxyl group with a basic surface oxygen atom. On a B-cation-terminated surface, the oxygen atom of the alcohol group forms a Lewis acid−base interaction with a coordinatively unsaturated metal cation. These results suggest that the basic surface oxygen atom on an A-cation-terminated surface is involved in dehydrogenation, while the Lewis acid site on a B-cation-terminated surface is involved in dehydration. Although the surface of the perovskites has a larger proportion of SrO or BaO than TiO or ZrO, the presence of both Lewis acid and basic surface oxygen atom in close proximity can be expected. The positive trend between the experimental and average DFT adsorption energy of 2-propanol further supports the presence of a heterogeneous surface (Figure S7). On the basis of DFT calculations, the dehydration of 2-propanol over perovskite catalysts is likely to occur via the E_2 and E_{1cB} mechanism, although the former pathway is expected to occur to a small extent as most of the Lewis acid sites are weakly acidic (Figure S4). The dehydrogenation of 2-propanol can only occur through the E_{1cB} pathway.

4.4. Trends in Acid−Base Catalysis Using Perovskites. As shown in Scheme 2, acid−base catalysis of 2-propanol over perovskite catalysts involves the adsorption of the reactant on an active site, the dissociation of the proton from the alcohol group to form a surface intermediate, and the formation of the adsorbed products, followed by desorption. Reactions involving solely acidic sites, such as the dehydration of methanol and glycerol, can be described by the strength of the acid sites and the ratio of Lewis to Brønsted acid sites, respectively.[80−82] However, in the presence of a base site, these reactivity descriptors are incomplete since the rate of reaction depends on the interaction of the acid and base sites with surface intermediates. To date, descriptors that account for acid−base catalysis over perovskite catalysts remain unavailable in the literature.

Reaction rates obtained experimentally reflect the free energy differences between the transition states and the respective precursor states.[83,84] As such, reactivity descriptors should reflect the free energy differences associated with the composition and structure of the catalysts. The Brønsted−Evans−Polanyi (BEP) relationship[85,86] states that the surface activation energy ($\Delta E_{act,surface}$) of an elementary reaction step is directly proportional to $\Delta H_{rxn,surface}$ and that it allows the estimation of activation barriers from surface heat of reactions for catalysts with similar surface geometries.[87−92] Therefore, we propose that $\Delta \hat{H}_{rxn,surface}$ may be used as a potential descriptor to compare reactivity trends among different perovskite catalysts at various temperatures. The plots in Figure 11 show that $\Delta \hat{H}_{rxn,surface}$, obtained from the measured heat of adsorption of 2-propanol and acetone at room temperature, correlates with the synthesis rate of acetone over the three perovskites ($SrZrO_3$ does not fit the trends due to its orthorhombic crystal structure). The correlations show that the rate of dehydrogenation increases with lower $\Delta E_{act,surface}$, which is due to the fact that the energy barrier to reach the transition state is lowered for perovskites with lower $\Delta E_{act,surface}$.

However, there are limitations in using $\Delta \hat{H}_{rxn,surface}$ as a reactivity descriptor. First, only the initial adsorption energy of 2-propanol and acetone measured at room temperature is used in our calculation of $\Delta \hat{H}_{rxn,surface}$. However, under reaction conditions, the surface sites of the catalysts are not vacant. As such, the relevant differential heats of adsorption at actual coverage under reaction conditions should be considered. Second, a distribution of active sites is expected to contribute to the observed reaction rate, resulting in a range of $\Delta \hat{H}_{rxn,surface}$. These two factors must be considered in order to develop a robust reactivity descriptor. As such, further work is required to verify that the surface heat of reaction can be used as a definite reactivity descriptor for acid−base catalysis by perovskites.

5. CONCLUSION

For the first time, we provided in this work a detailed investigation and understanding on the surface acid−base properties and reactivity of a series of selected perovskite catalysts and laid the groundwork for further exploration of perovskite catalysts in acid−base reactions. Characterization of the four perovskites, $SrTiO_3$, $BaTiO_3$, $SrZrO_3$, and $BaZrO_3$, revealed that these catalysts have a high ratio of intermediate and strong basic surface oxygen atoms to weak Lewis acid sites, after pretreatment at 550 °C in the presence of oxygen. This acid−base property is related to the fact that the surface of these perovskites is largely dominated by the AO layer (SrO or BaO) as measured by LEIS analysis. Using the conversion of 2-propanol as a probe reaction under steady state condition, these perovskites exhibit a high selectivity to acetone (>70%) compared to that of propene. On the basis of FTIR spectroscopy supported by DFT calculations, it is suggested that both dehydration and dehydrogenation reactions occur mainly through the E_{1cB} pathway, which involves the deprotonation of the alcohol group to form a common alkoxy intermediate. The displacement of the adsorption site on the A-cation-terminated surface and the adsorption energy of 2-propanol ($\Delta H_{ads,2\text{-}propanol}$) correlate linearly with the tolerance factor of the perovskites. This implies that the adsorption property of perovskites encompasses not only the synergy between surface acid and base sites but also the change in surface geometry imposed by the bulk structure. The work here manifests the importance of understanding not only the bulk

DOI: 10.1021/acscatal.7b00783
ACS Catal. 2017, 7, 4423−4434

structure but also the surface structure and composition for catalysis over complex oxides such as perovskites.

■ ASSOCIATED CONTENT

Supporting Information

The Supporting Information is available free of charge on the ACS Publications website at DOI: 10.1021/acscatal.7b00783.

Mass transfer limitation tests, FTIR spectra for the adsorption of pyridine and CO_2, carbonate mode assignment from CO_2 adsorption, adsorption and temperature-programmed reaction of 2-propanol followed by FTIR spectroscopy, heat of adsorption of acetone, DFT calculations of 2-propanol adsorption, comparison between experimental and average DFT adsorption energy of 2-propanol on perovskite catalysts, adsorption energy of molecular hydrogen on an A-cation-terminated surface, and derivation of surface heat of reaction (PDF)

■ AUTHOR INFORMATION

Corresponding Author

*E-mail: wuz1@ornl.gov.

ORCID

Victor Fung: 0000-0002-3347-6983
De-en Jiang: 0000-0001-5167-0731
Steven H. Overbury: 0000-0002-5137-3961
Zili Wu: 0000-0002-4468-3240

Author Contributions

§G.S.F and F.P.G contributed equally to this work.

Notes

The authors declare no competing financial interest.

■ ACKNOWLEDGMENTS

This research is sponsored by the U.S. Department of Energy, Office of Science, Office of Basic Energy Sciences, Chemical Sciences, Geosciences, and Biosciences Division. Part of the work including SEM, XRD, FTIR spectroscopy, and kinetic measurement was conducted at the Center for Nanophase Materials Sciences, which is a DOE Office of Science User Facility. This research used resources of the National Energy Research Scientific Computing Center, a DOE Office of Science User Facility supported by the Office of Science of the U.S. Department of Energy under Contract No. DE-AC02-05CH11231. We thank Henry Luftman (Lehigh University) for performing the LEIS analysis, Yubing Lu and Ayman Karim (Virginia Tech) for providing the design of the stand for connecting the microcalorimeter to the adsorption instrument, Aditya Ashi Savara (ORNL) for fruitful discussions, and Elizabeth E. Bickel (Undergraduate Student at Tennessee Technological University) for helping data collection during a summer internship at Oak Ridge National Laboratory under the SULI (Science Undergraduate Laboratory Internships) program 2016.

■ REFERENCES

(1) Zhu, H.; Zhang, P.; Dai, S. *ACS Catal.* **2015**, *5*, 6370−6385.
(2) Zhu, J.; Li, H.; Zhong, L.; Xiao, P.; Xu, X.; Yang, X.; Zhao, Z.; Li, J. *ACS Catal.* **2014**, *4*, 2917−2940.
(3) Royer, S.; Duprez, D.; Can, F.; Courtois, X.; Batiot-Dupeyrat, C.; Laassiri, S.; Alamdari, H. *Chem. Rev.* **2014**, *114*, 10292−10368.
(4) Sato, T.; Takagi, S.; Deledda, S.; Hauback, B. C.; Orimo, S.-i. *Sci. Rep.* **2016**, *6*, 23592.
(5) Libby, W. F. *Science* **1971**, *171*, 499−500.
(6) Voorhoeve, R. J.; Remeika, J. P.; Johnson, D. W. *Science* **1973**, *180*, 62−64.
(7) Belessi, V. C.; Trikalitis, P. N.; Ladavos, A. K.; Bakas, T. V.; Pomonis, P. J. *Appl. Catal., A* **1999**, *177*, 53−68.
(8) Zhang, R.; Luo, N.; Yang, W.; Liu, N.; Chen, B. *J. Mol. Catal. A: Chem.* **2013**, *371*, 86−93.
(9) Hansen, K. K.; Skou, E. M.; Christensen, H.; Turek, T. *J. Catal.* **2001**, *199*, 132−140.
(10) Ferri, D.; Forni, L.; Dekkers, M. A. P.; Nieuwenhuys, B. E. *Appl. Catal., B* **1998**, *16*, 339−345.
(11) Zhao, Z.; Yang, X. G.; Wu, Y. *Appl. Catal., B* **1996**, *8*, 281−297.
(12) Zhu, J.; Yang, X.; Xu, X.; Wei, K. *J. Phys. Chem. C* **2007**, *111*, 1487−1490.
(13) Zhang, R. D.; Villanueva, A.; Alamdari, H.; Kaliaguine, S. *J. Catal.* **2006**, *237*, 368−380.
(14) Royer, S.; Duprez, D. *ChemCatChem* **2011**, *3*, 24−65.
(15) Castellazzi, P.; Groppi, G.; Forzatti, P.; Baylet, A.; Marecot, P.; Duprez, D. *Catal. Today* **2010**, *155*, 18−26.
(16) Royer, S.; Ayrault, C.; Carnevillier, C.; Epron, F.; Marecot, P.; Duprez, D. *Catal. Today* **2006**, *117*, 543−548.
(17) Ponce, S.; Pena, M. A.; Fierro, J. L. G. *Appl. Catal., B* **2000**, *24*, 193−205.
(18) Trikalitis, P. N.; Pomonis, P. J. *Appl. Catal., A* **1995**, *131*, 309−322.
(19) Cyganiuk, A.; Klimkiewicz, R.; Lukaszewicz, J. P. *Mater. Res. Bull.* **2011**, *46*, 327−332.
(20) Kuhn, J. N.; Ozkan, U. S. *J. Catal.* **2008**, *253*, 200−211.
(21) Natile, M. M.; Ugel, E.; Maccato, C.; Glisenti, A. *Appl. Catal., B* **2007**, *72*, 351−362.
(22) Aramendía, M. A.; Borau, V.; Jiménez, C.; Marinas, J. M.; Porras, A.; Urbano, F. J. *J. Catal.* **1996**, *161*, 829−838.
(23) Gervasini, A.; Auroux, A. *J. Catal.* **1991**, *131*, 190−198.
(24) Rekoske, J. E.; Barteau, M. A. *J. Catal.* **1997**, *165*, 57−72.
(25) Brunauer, S.; Emmett, P. H.; Teller, E. *J. Am. Chem. Soc.* **1938**, *60*, 309−319.
(26) Barrett, E. P.; Joyner, L. G.; Halenda, P. P. *J. Am. Chem. Soc.* **1951**, *73*, 373−380.
(27) Ushakov, S. V.; Navrotsky, A. *Appl. Phys. Lett.* **2005**, *87*, 164103.
(28) Wu, D.; Guo, X.; Sun, H.; Navrotsky, A. *J. Phys. Chem. C* **2015**, *119*, 15428−15433.
(29) ter Veen, H. R. J.; Kim, T.; Wachs, I. E.; Brongersma, H. H. *Catal. Today* **2009**, *140*, 197−201.
(30) Phivilay, S. P.; Puretzky, A. A.; Domen, K.; Wachs, I. E. *ACS Catal.* **2013**, *3*, 2920−2929.
(31) Kresse, G.; Furthmüller, J. *Comput. Mater. Sci.* **1996**, *6*, 15−50.
(32) Kresse, G.; Furthmuller, J. *Phys. Rev. B: Condens. Matter Mater. Phys.* **1996**, *54*, 11169−11186.
(33) Perdew, J. P.; Burke, K.; Ernzerhof, M. *Phys. Rev. Lett.* **1996**, *77*, 3865−3868.
(34) Kresse, G.; Joubert, D. *Phys. Rev. B: Condens. Matter Mater. Phys.* **1999**, *59*, 1758−1775.
(35) Blochl, P. E. *Phys. Rev. B: Condens. Matter Mater. Phys.* **1994**, *50*, 17953−17979.
(36) Monkhorst, H. J.; Pack, J. D. *Phys. Rev. B* **1976**, *13*, 5188−5192.
(37) Dong, L.; Luo, Q.; Cheng, K.; Shi, H.; Wang, Q.; Weng, W.; Han, W.-Q. *Sci. Rep.* **2015**, *4*, 5084.
(38) Mu, L.; Zhao, Y.; Li, A.; Wang, S.; Wang, Z.; Yang, J.; Wang, Y.; Liu, T.; Chen, R.; Zhu, J.; Fan, F.; Li, R.; Li, C. *Energy Environ. Sci.* **2016**, *9*, 2463−2469.
(39) Tsumura, T.; Matsuoka, K.; Toyoda, M. *J. Mater. Sci. Technol.* **2010**, *26*, 33−38.
(40) Mao, Y.; Banerjee, S.; Wong, S. S. *J. Am. Chem. Soc.* **2003**, *125*, 15718−15719.
(41) Zhou, H.; Mao, Y.; Wong, S. S. *J. Mater. Chem.* **2007**, *17*, 1707−1713.

DOI: 10.1021/acscatal.7b00783
ACS Catal. 2017, 7, 4423−4434

(42) Kumar, H. P.; Vijayakumar, C.; George, C. N.; Solomon, S.; Jose, R.; Thomas, J. K.; Koshy, J. *J. Alloys Compd.* **2008**, *458*, 528−531.
(43) Evans, S. E.; Staniforth, J. Z.; Darton, R. J.; Ormerod, R. M. *Green Chem.* **2014**, *16*, 4587−4594.
(44) Gupta, S. K.; Ghosh, P. S.; Pathak, N.; Arya, A.; Natarajan, V. *RSC Adv.* **2014**, *4*, 29202−29215.
(45) Bhatia, S. K.; Myers, A. L. *Langmuir* **2006**, *22*, 1688−1700.
(46) Lavrich, D. J.; Wetterer, S. M.; Bernasek, S. L.; Scoles, G. *J. Phys. Chem. B* **1998**, *102*, 3456−3465.
(47) Lercher, J. A.; Grundling, C.; EderMirth, G. *Catal. Today* **1996**, *27*, 353−376.
(48) Tamura, M.; Shimizu, K.-i.; Satsuma, A. *Appl. Catal., A* **2012**, *433*−*434*, 135−145.
(49) Lundie, D. T.; McInroy, A. R.; Marshall, R.; Winfield, J. M.; Jones, P.; Dudman, C. C.; Parker, S. F.; Mitchell, C.; Lennon, D. *J. Phys. Chem. B* **2005**, *109*, 11592−11601.
(50) Lercher, J. A.; Colombier, C.; Noller, H. *J. Chem. Soc., Faraday Trans. 1* **1984**, *80*, 949−959.
(51) Copeland, J. R.; Santillan, I. A.; Schimming, S. M.; Ewbank, J. L.; Sievers, C. *J. Phys. Chem. C* **2013**, *117*, 21413−21425.
(52) Di Cosimo, J. I.; Diez, V. K.; Xu, M.; Iglesia, E.; Apesteguia, C. R. *J. Catal.* **1998**, *178*, 499−510.
(53) del Arco, M.; Gutierrez, S.; Martin, C.; Rives, V. *Phys. Chem. Chem. Phys.* **2001**, *3*, 119−126.
(54) Fuente, S. A.; Ferretti, C. A.; Domancich, N. F.; Diez, V. K.; Apesteguia, C. R.; Di Cosimo, J. I.; Ferullo, R. M.; Castellani, N. J. *Appl. Surf. Sci.* **2015**, *327*, 268−276.
(55) Kooli, F.; Martin, C.; Rives, V. *Langmuir* **1997**, *13*, 2303−2306.
(56) Martin, C.; Martin, I.; Rives, V.; Grzybowska, B.; Gressel, I. *Spectrochim. Acta, Part A* **1996**, *52*, 733−740.
(57) Socrates, G. *Infrared and Raman Characteristic Group Frequencies: Tables and Charts*, 3rd ed.; Wiley: Chichester, England, 2001; p 50.
(58) Sano, T.; Saylor, D. M.; Rohrer, G. S. *J. Am. Ceram. Soc.* **2003**, *86*, 1933−1939.
(59) Sano, T.; Kim, C. S.; Rohrer, G. S. *J. Am. Ceram. Soc.* **2005**, *88*, 993−996.
(60) Erdman, N.; Poeppelmeier, K. R.; Asta, M.; Warschkow, O.; Ellis, D. E.; Marks, L. D. *Nature* **2002**, *419*, 55−58.
(61) Deak, D. *Mater. Sci. Technol.* **2007**, *23*, 127−136.
(62) Eglitis, R.; Vanderbilt, D. *Phys. Rev. B: Condens. Matter Mater. Phys.* **2008**, *78*, 155420.
(63) Eglitis, R.; Vanderbilt, D. *Phys. Rev. B: Condens. Matter Mater. Phys.* **2007**, *76*, 155439.
(64) Tesquet, G.; Faye, J.; Hosoglu, F.; Mamede, A.-S.; Dumeignil, F.; Capron, M. *Appl. Catal., A* **2016**, *511*, 141−148.
(65) Sahu, S. K.; Zlotnik, S.; Navrotsky, A.; Vilarinho, P. M. *J. Mater. Chem. C* **2015**, *3*, 7691−7698.
(66) Goniakowski, J.; Bouette-Russo, S.; Noguera, C. *Surf. Sci.* **1993**, *284*, 315−327.
(67) Erdman, N.; Warschkow, O.; Asta, M.; Poeppelmeier, K. R.; Ellis, D. E.; Marks, L. D. *J. Am. Chem. Soc.* **2003**, *125*, 10050−10056.
(68) Meyerheim, H. L.; Ernst, A.; Mohseni, K.; Maznichenko, I. V.; Ostanin, S.; Klimenta, F.; Jedrecy, N.; Feng, W.; Mertig, I.; Felici, R.; Kirschner, J. *Phys. Rev. Lett.* **2012**, *108*, 215502.
(69) Sambrano, J. R.; Longo, V. M.; Longo, E.; Taft, C. A. *J. Mol. Struct.: THEOCHEM* **2007**, *813*, 49−56.
(70) Ho, J.; Heifets, E.; Merinov, B. *Surf. Sci.* **2007**, *601*, 490−497.
(71) Dagdeviren, O. E.; Simon, G. H.; Zou, K.; Walker, F. J.; Ahn, C.; Altman, E. I.; Schwarz, U. D. *Phys. Rev. B: Condens. Matter Mater. Phys.* **2016**, *93*, 195303.
(72) Miyata, H.; Wakamiya, M.; Kubokawa, Y. *J. Catal.* **1974**, *34*, 117−123.
(73) Varadarajan, T. K.; Sumathi, R.; Viswanathan, B. *Indian J. Chem. Sect A-Inorg. Bio-Inorg. Phys. Theor. Anal. Chem.* **2001**, *40*, 1033−1036.
(74) Díez, V. K.; Apesteguía, C. R.; Di Cosimo, J. I. *Catal. Today* **2000**, *63*, 53−62.
(75) Díez, V. K.; Apesteguía, C. R.; Di Cosimo, J. I. *J. Catal.* **2003**, *215*, 220−233.
(76) Larmier, K.; Chizallet, C.; Maury, S.; Cadran, N.; Abboud, J.; Lamic-Humblot, A.-F.; Marceau, E.; Lauron-Pernot, H. *Angew. Chem., Int. Ed.* **2017**, *56*, 230−234.
(77) Baylon, R. A. L.; Sun, J.; Martin, K. J.; Venkitasubramanian, P.; Wang, Y. *Chem. Commun.* **2016**, *52*, 4975−4978.
(78) Sun, J.; Baylon, R. A. L.; Liu, C.; Mei, D.; Martin, K. J.; Venkitasubramanian, P.; Wang, Y. *J. Am. Chem. Soc.* **2016**, *138*, 507−517.
(79) Ramasamy, K. K.; Gray, M.; Job, H.; Smith, C.; Wang, Y. *Catal. Today* **2016**, *269*, 82−87.
(80) Alharbi, W.; Kozhevnikova, E. F.; Kozhevnikov, I. V. *ACS Catal.* **2015**, *5*, 7186−7193.
(81) Jones, A. J.; Carr, R. T.; Zones, S. I.; Iglesia, E. *J. Catal.* **2014**, *312*, 58−68.
(82) Foo, G. S.; Wei, D.; Sholl, D. S.; Sievers, C. *ACS Catal.* **2014**, *4*, 3180−3192.
(83) Jones, A. J.; Iglesia, E. *Angew. Chem., Int. Ed.* **2014**, *53*, 12177−12181.
(84) Deshlahra, P.; Iglesia, E. *ACS Catal.* **2016**, *6*, 5386−5392.
(85) Evans, M. G.; Polanyi, M. *Trans. Faraday Soc.* **1938**, *34*, 11−24.
(86) Bell, R. P. *Proc. R. Soc. London, Ser. A* **1936**, *154*, 414−429.
(87) Norskov, J. K.; Bligaard, T.; Rossmeisl, J.; Christensen, C. H. *Nat. Chem.* **2009**, *1*, 37−46.
(88) Abild-Pedersen, F.; Greeley, J.; Studt, F.; Rossmeisl, J.; Munter, T. R.; Moses, P. G.; Skúlason, E.; Bligaard, T.; Nørskov, J. K. *Phys. Rev. Lett.* **2007**, *99*, 016105.
(89) Ferrin, P.; Simonetti, D.; Kandoi, S.; Kunkes, E.; Dumesic, J. A.; Nørskov, J. K.; Mavrikakis, M. *J. Am. Chem. Soc.* **2009**, *131*, 5809−5815.
(90) Michaelides, A.; Liu, Z. P.; Zhang, C. J.; Alavi, A.; King, D. A.; Hu, P. *J. Am. Chem. Soc.* **2003**, *125*, 3704−3705.
(91) Nørskov, J. K.; Bligaard, T.; Logadottir, A.; Bahn, S.; Hansen, L. B.; Bollinger, M.; Bengaard, H.; Hammer, B.; Sljivancanin, Z.; Mavrikakis, M.; Xu, Y.; Dahl, S.; Jacobsen, C. J. H. *J. Catal.* **2002**, *209*, 275−278.
(92) Polo-Garzon, F.; He, M.; Bruce, D. A. *J. Catal.* **2016**, *333*, 59−70.

DOI: 10.1021/acscatal.7b00783
ACS Catal. 2017, 7, 4423−4434